

Sediment flux from the morphodynamics of elongating linear dunes

Antoine Lucas, Clément Narteau, Sébastien Rodriguez,
Olivier Rozier, Yann Callot, Amandine Garcia, Sylvain Courrech du Pont

September 14, 2015

Supplementary Information

Contents

1	Field measurements in the Fachi-Bilma erg (1976)	2
2	Imagery analysis over the Fachi-Bilma erg from 1957 to 2014	5
3	Modeling linear dune growth and sediment flux assessment	13

1 Field measurements in the Fachi-Bilma erg (1976)

The Fachi-Bilma erg has been explored by Yann Callot (YC) in 1976 [1]. Along with mapping, he took photographs from the field and sampled the sand at different locations. Fig. S1 is taken North from Fachi, Niger ($18^{\circ} 10'N$, $11^{\circ} 37'E$) and shows a silk growing downwind of a hill (i.e., lee dune) and extending westwards. As shown, the linear dune crest is visible along the slope of the relief indicating the presence of a major zone of deposition (see also Fig. DR15). The picture taken from the apex of a seif dune illustrates the complex morphology along the crest (Fig. DR2). Locally, the slope ranges from few degrees up to the angle of repose (i.e., $\sim 30^{\circ}$) where avalanches are observed on the lee sides (see Fig. DR3). Pictures also suggest that the grain sizes differ between the dune and the interdune areas (see Figs. DR4a-b). Indeed, granulometric measurements show that the dunes are made of finest grains compared to the interdune areas with a D_{50} equal to 180 and 600 μm , respectively (Fig. DR4c). This illustrates that linear dunes evolve on a non-mobilizable sediment bed.

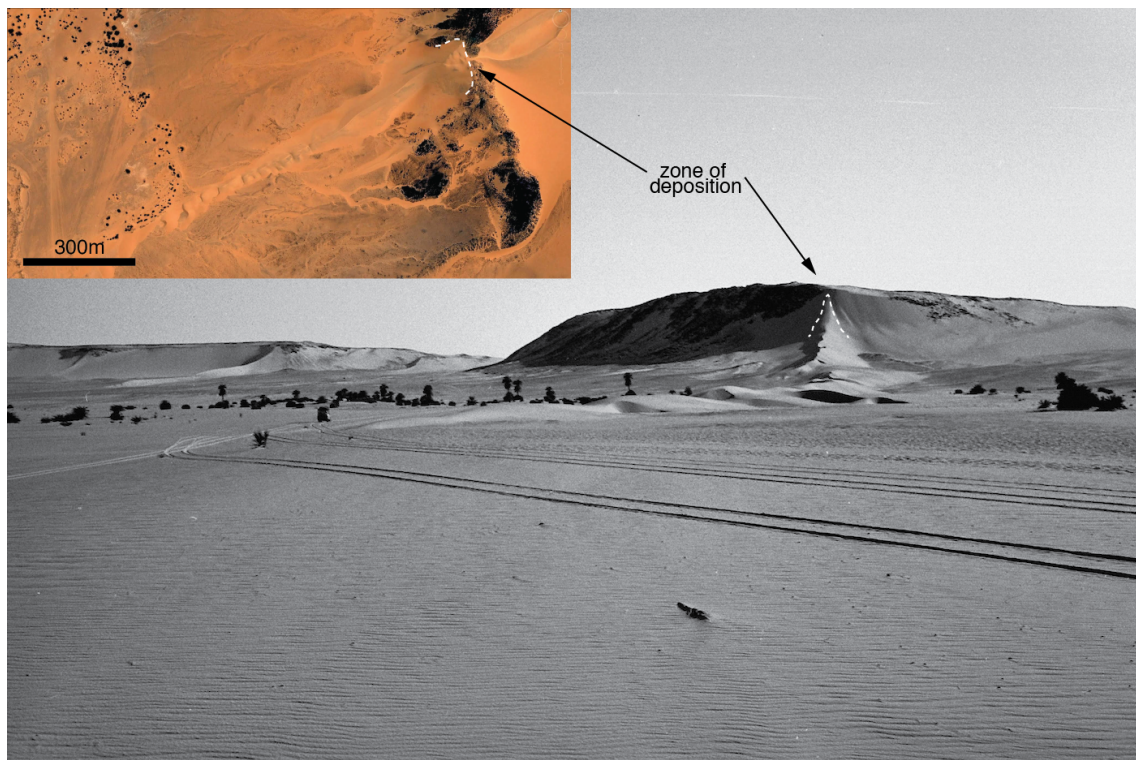


Figure DR1: Linear dune elongation from a topographic obstacle ($18^{\circ}10'N$, $11^{\circ}37'E$). This example shows that a zone of deposition forms along the downwind slope of the obstacle. This results in the formation of a lee dune, from which the linear dune nucleates and propagates (picture taken in 1976 by YC). Inset shows a Digital-Globe satellite imagery taken in June 2004.



Figure DR2: Undulation, crestline and ripples ($18^{\circ}10'N$, $11^{\circ}39'E$). The width of this silk is about 20 meters. Note that the top is flat in some places whereas steep slopes with a sharp crestline can be seen in the background (picture taken in 1976 by YC). On the foreground, ripples are observed on the windward sides of the linear dunes.

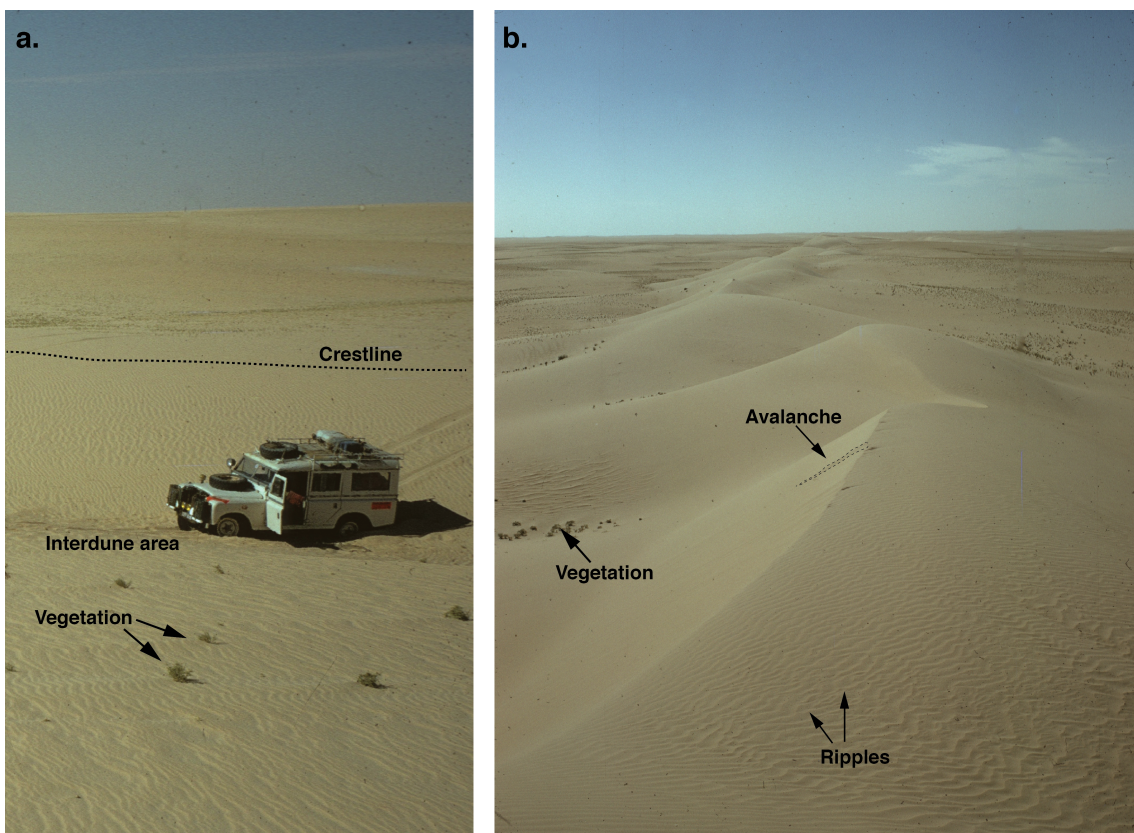


Figure DR3: Linear dune morphology in the erg of Fachi-Bilma ($18^{\circ}10'N$, $11^{\circ}39'E$). **a.** The linear dunes reach ~ 10 m when observed away from the tip. Sparse vegetation is present in the interdune area. **b.** Avalanches occasionally occur on the lee sides when the angle of repose is reached. Slopes range between $\sim 10^{\circ}$ and the angle of repose (picture taken in 1976 by YC). Ripples are observed on the windward sides.

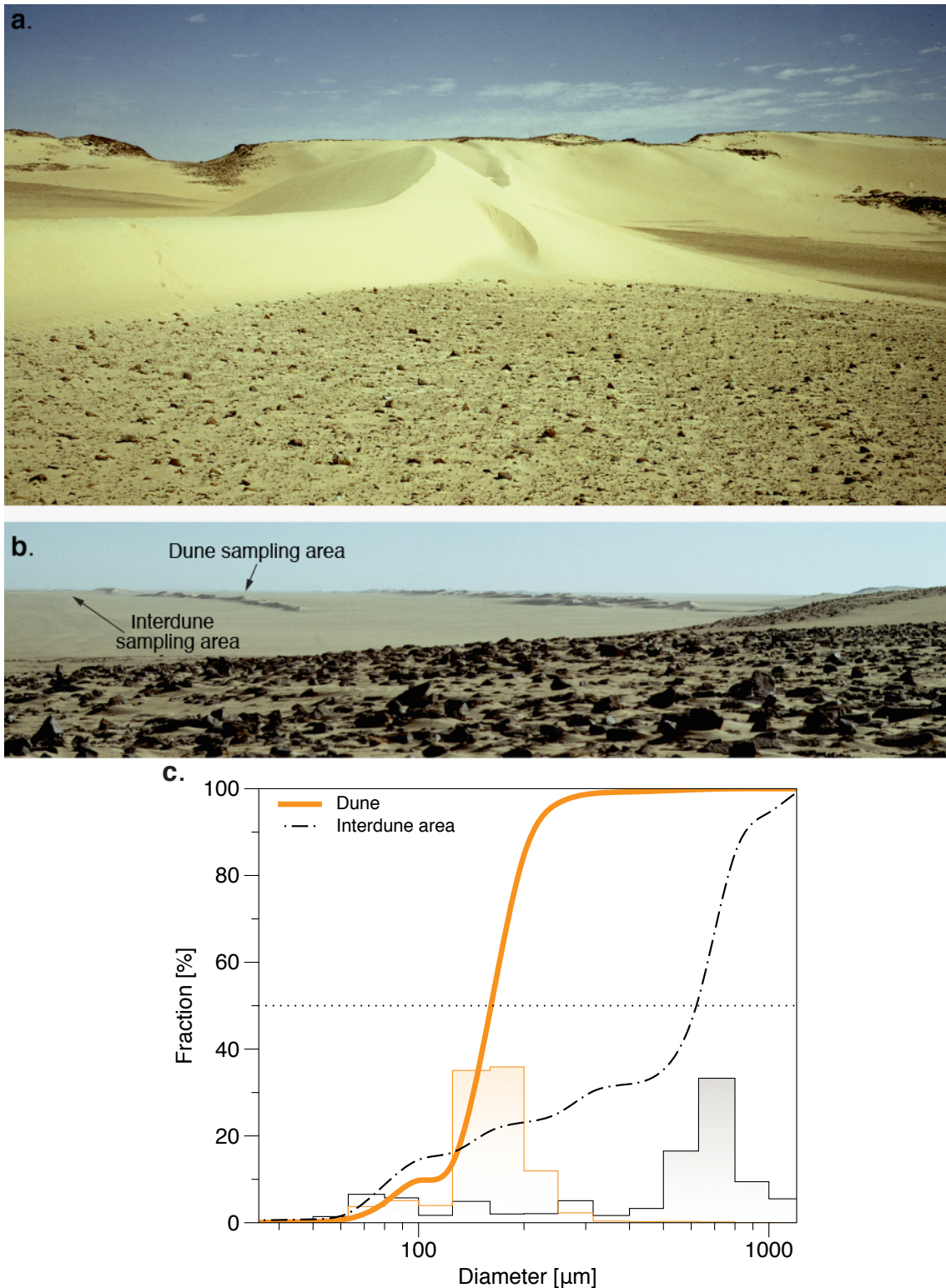


Figure DR4: Granulometry of the dunes and interdune areas. **a.** Field pictures showing the interdune areas covered by coarse grains while the dunes are composed of smaller grains. **b.** Wide range picture of finger-like dunes where the granulometry sampling has been performed ($18^{\circ}10'N$, $11^{\circ}39'E$). **c.** Granulometry distributions from the field near the silk shown in panel **b.** (pictures taken in 1976 by YC). The lines and the histograms show cumulative and probability distribution functions, respectively. This difference in grain size suggests that linear dunes develop on a non-mobilisable bed.

2 Imagery analysis over the Fachi-Bilma erg from 1957 to 2014

Archives from Landsat and aerial photographs from IGN (1957) along with Google Earth imagery have been used for mapping the linear dunes and estimate their elongation rates. Google Earth offers recent data with resolution of few meters (2005-2014). LandSat and IGN's images have been used for older times (1957-2010). These images allow mapping of linear dunes (see Figs. DR5-S7).

None of the existing data sets were able to resolve the height of these linear dunes, at the time of the study. Therefore we requested a Pléiades acquisition over our region of interest (Fig. DR8). Thanks to the French GEOSUD consortium and the associated ANR grants, we obtained a stereo pair during fall 2014. Using different photogrammetry solutions (e.g., NASA AMES Stereo Pipeline [2], BAE System SOCET GXP and ENS-CMLA S2P [3]) we were able to derive and compare digital elevation models (DEM) (see close up on the 3D cloud on Fig. S8). The comparison is shown in the supplementary Fig. DR9. We also test the the sensitivity of the retrieved DEM to the photogrammetry settings (namely the correlation parameters). One resulting profile is given in Fig. DR10. Our tests show that the difference in the correlation settings lead to a mean standard deviation of 26 cm on the dune height estimation with a maximum value that does not exceed 50 cm.

Along with the noise in our DEM, another source of variations comes from the complex morphology of the linear dunes (see supplementary Figs. DR1-S4). We observe sharp crest-lines with avalanche slopes in some areas, while in others dunes exhibit smoother and lower slope, as shown in the topographic profile stacked along the crest-line direction on the supplementary Fig. DR11.

Using the 3D cloud derived from the Pléiades stereo pair, we computed height, width and cross-section of the dunes along the first 100 meters from their tips using overlapping sliding rectangular box of 2.5 meters width along the crestline directions (see Fig. DR12a). The cross-section versus height \times width relationship falls in between a parabolic and triangular shape (Fig. DR12b) with a characteristic aspect ratio of 0.3 as discussed in the main text. This is attested by the morphology observed on the field and previously shown on Figs. DR1-DR4. When no topography is available, it is therefore possible to assess sediment flux by using the simple relationship $Q = eS/W = eAW$ (see main text). Here we show that the mean factor A has a mean of 0.11 with a minimum of 0.05 and a maximum of 0.28 from our data.

Figure DR5: Animated sequence of imagery from 1957 to 2013 over the Bilma area. Reader will need an pdf reader that handles multimedia plugins and JavaScript (i.e., Adobe Acrobat). This sequence is also shown on Fig. DR6.

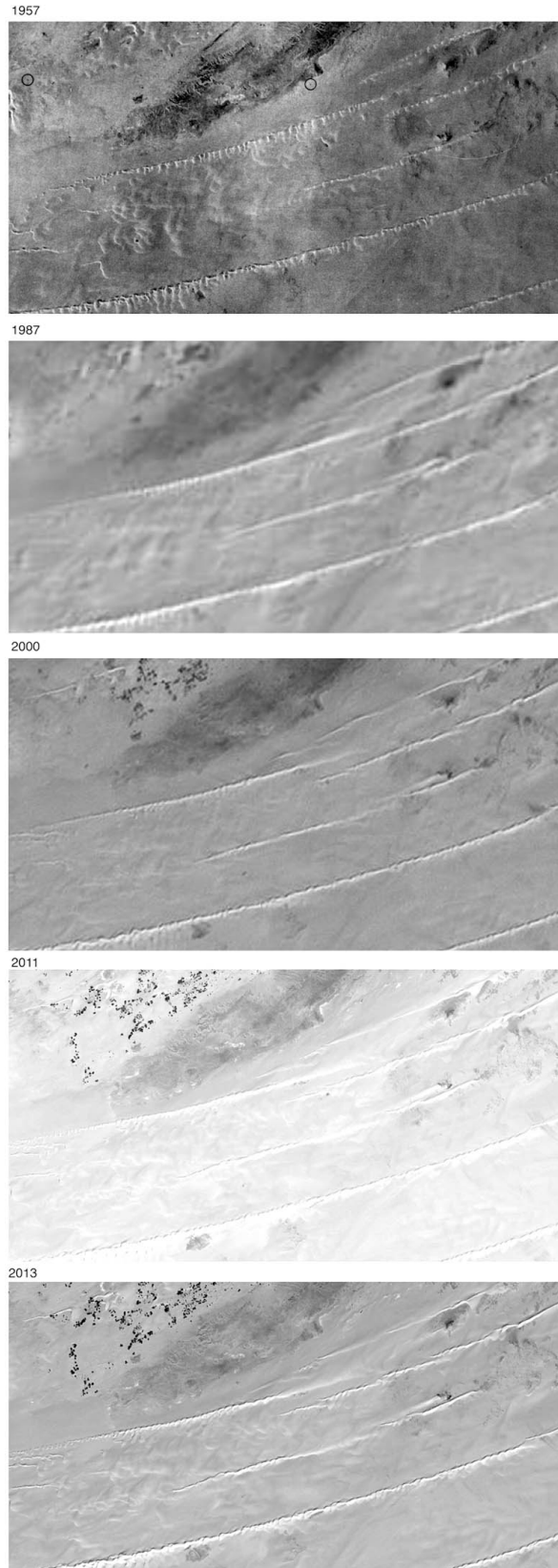


Figure DR6: Sequence of co-registered satellite images from 1957 to 2013. Despite possible changes in dune shape (i.e., barchans ejection, change in lee front orientation etc.), linear dunes have not migrated laterally by more than 2 meters over 56 years. As clearly observed in 1957, the linear dune may break into a train of barchans under a constant wind conditions. Associated mapping is shown on Fig. DR7.

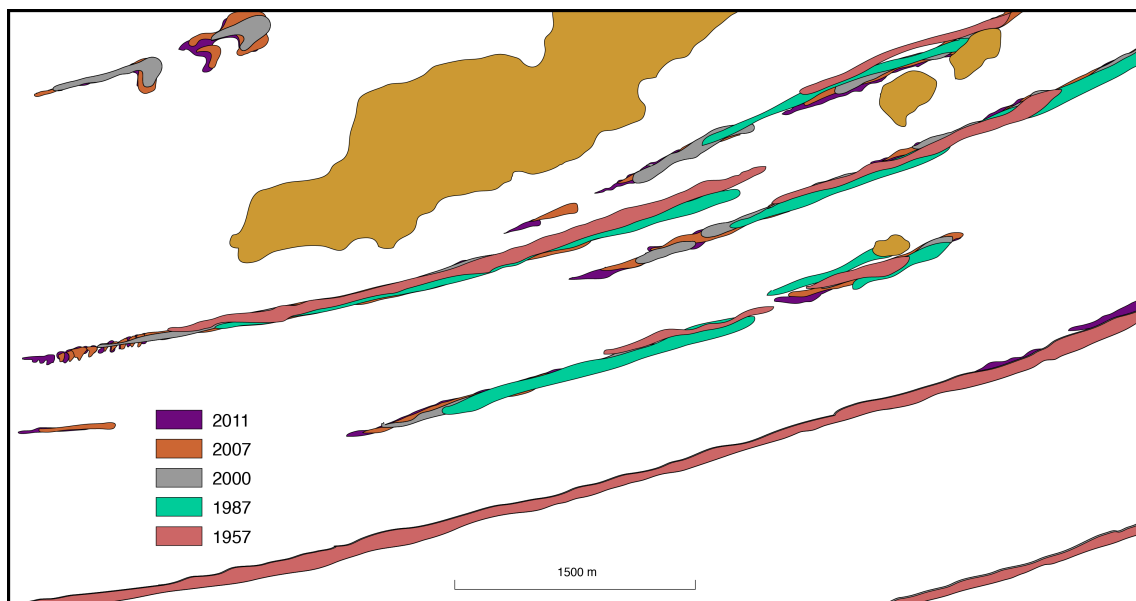


Figure DR7: Mapping of the sequenced images from 1957 to 2011. Over more than 50 years, imagery from IGN aerial photography (1956), LandSat (1976-2010), DigitalGlobe from Google Earth image (2003-2011) show that silks do not present any lateral migration but only elongation in one direction (see Figs. DR5 and DR6). The close-up shown in Fig. 2 of the main text illustrates that the crest lines stand in their original alignment with no lateral translation.

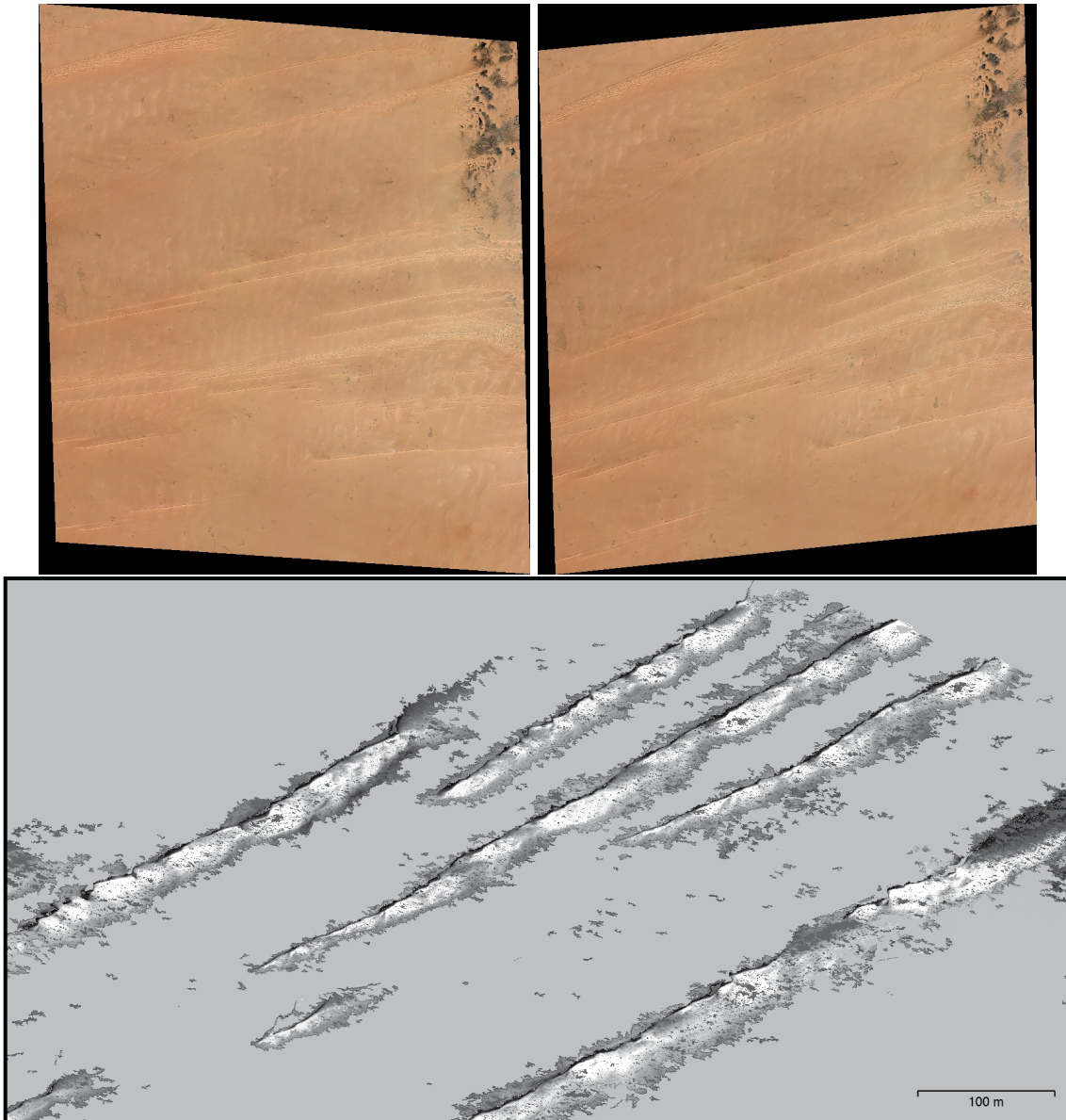


Figure DR8: PI'eiades stereo pair and the derived shaded altimetric 3D cloud over linear dunes. (top) the PI'eiades stereo pair. (bottom) The 3D cloud focused on linear dunes' tip. Uncertainties assessment is illustrated on Figs. DR9 and DR10.

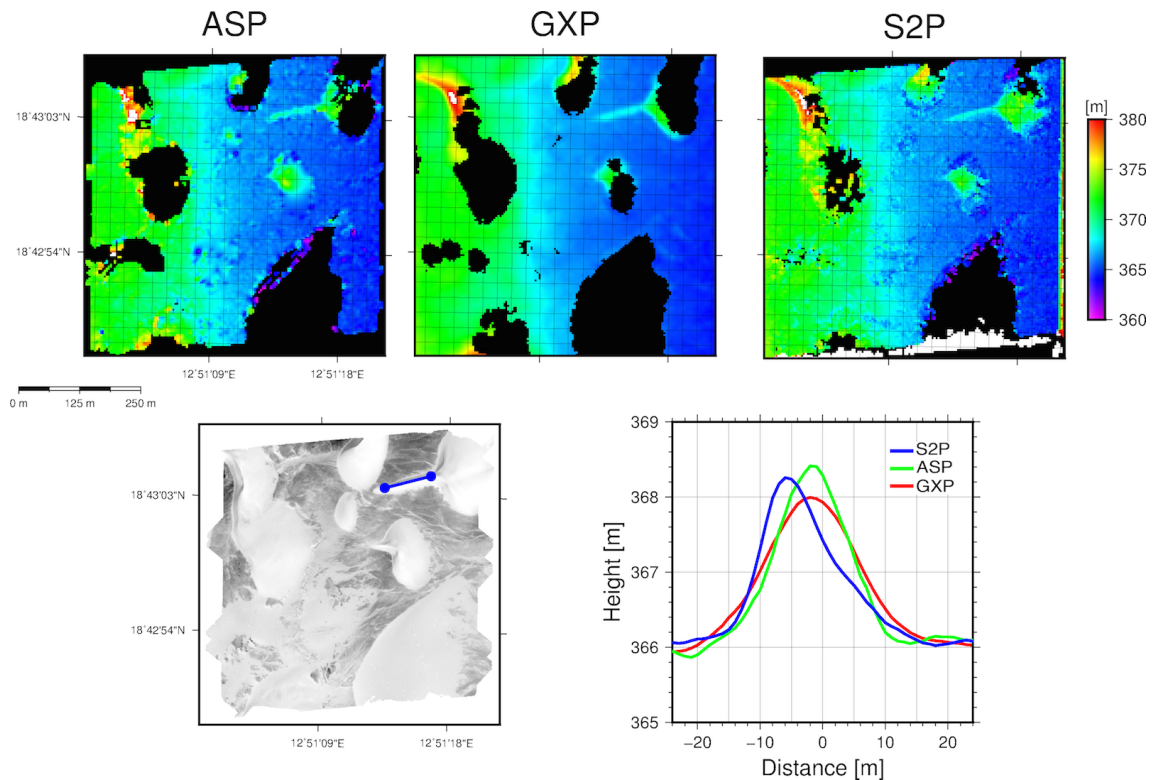


Figure DR9: Comparison of photogrammetric solutions on the Píeiades stereo pair.(top figures) Comparison of three photogrammetric methods including NASA Ames Stereo Pipeline (ASP), the commercial SOCET GXP from BAE System (GXP), and CMLA-S2P (S2P). The whole scene has been treated and projected in UTM zone 33Q. Blank (white and black) areas correspond to low correlation and inaccurate height retrieval, and have been rejected. The bottom-left figure is the corresponding orthoimage. The blue line indicate the crestline over which 50 cross-section profiles have been stacked and compared. For each photogrammetric solution, these profiles are shown in the bottom-right figure.

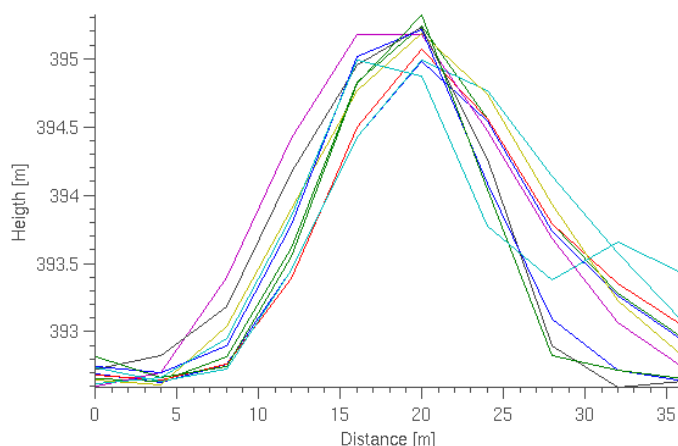


Figure DR10: Correlation setting effects on the DEM derivation. Comparison of the same cross-section profile over a silk dune while using different correlation parameters including windows size, sub-pixel kernel size, correlation threshold and pre-processing filtering. This leads to a mean standard deviation of 26 cm over the dunes with a maximum value that does not exceed 50 cm. In terms of relative elevation, the effects of correlation settings imply dif-ferences of less than 35 cm, which leads to an uncertainty of 10% on the estimated thickness of the silk at a given profile. We therefore stacked along the crest-line track +10 of profiles in order to reduce this error, giving us a good confidence on our heights measurements (see Fig. DR9).

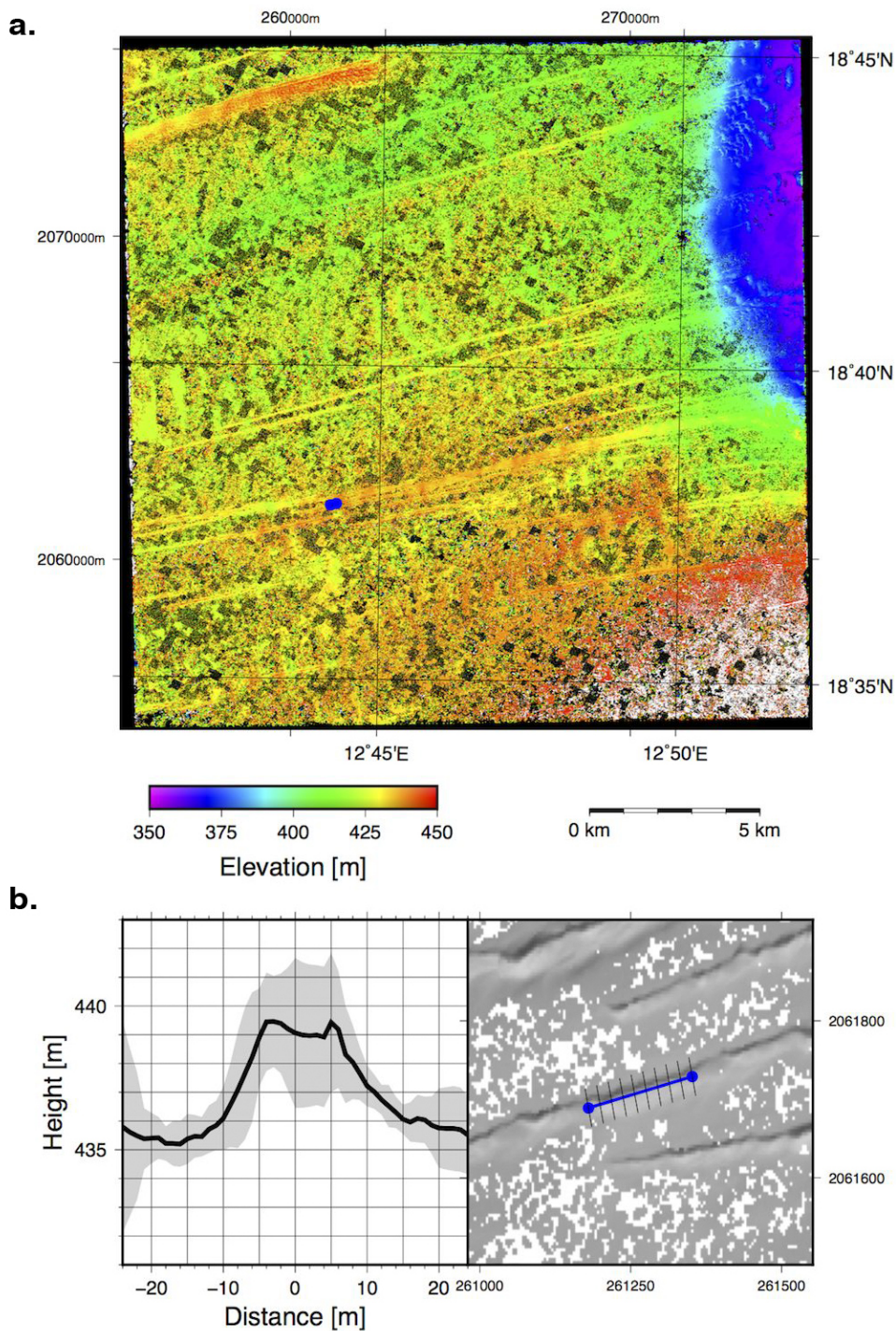


Figure DR11: Digital elevation model and cross-section over linear dunes of the erg of Fachi-Bilma from PI'eiades stereo pair. a. The main map covers the PI'eiades scene in UTM projection. **b.** For an individual dune, the blue dots indicates the end points of the profile. Different cross-sections (shown in black of the top-right inset) have been stacked along the main profile (blue line in the top-right inset). The gray area corresponds to the range of cross-section profile variation. The black line is the average profile across a linear dune.

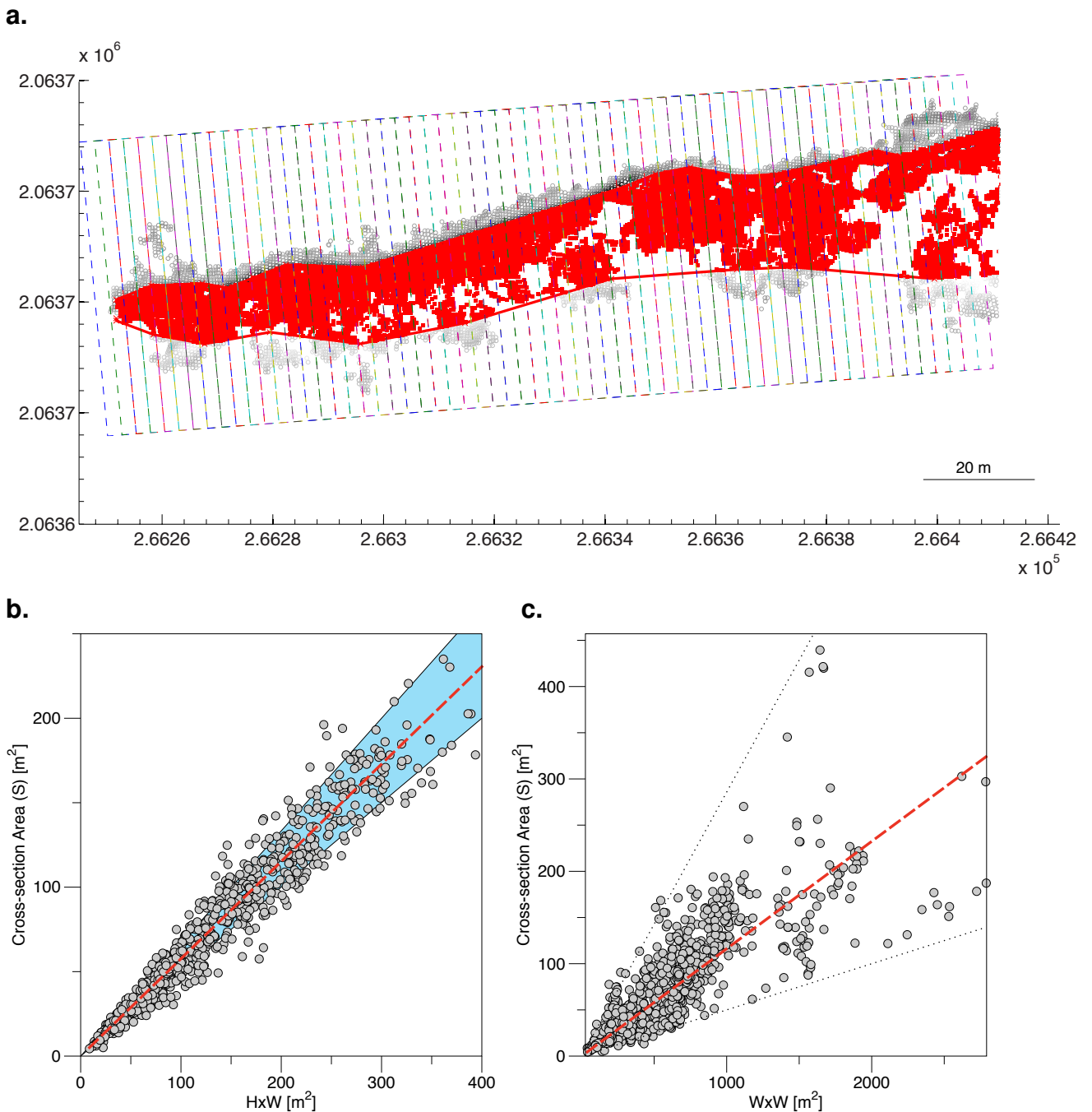


Figure DR12: Morphological metrics of linear dunes of the erg of Fachi-Bilma extracted from 3D altimetric cloud. a. Overlapping sliding rectangular box (dashed contour) of 2.5 meters width along the crestline direction over the 3D altimetric cloud derived from the Pléiades stereo pair are used to extract the morphological properties of 80 linear dunes (see Fig. S8). The red dots fall inside the dune itself. **b.** The top and bottom black lines assume a parabolic shape ($S = 2/3W \times H$) and a triangular shape ($S = 1/2W \times H$), re-spectively. The best-fit trend falls in between the two geometries (dashed red line). The blue area corresponds to the region between the two end-member geometries and is very close to the 1-sigma window. **c.** Cross-section area as a function of the squared width (W), where $S = AW^2$. The mean factor A has a mean of 0.11.

3 Modeling linear dune growth and sediment flux assessment

The model named ReSCAL (Real-Space Cellular Automaton Laboratory) is an open-source package which has been described in full details in [4]. We recall here the main characteristics of the dune model [5], and detail of the numerical analysis relevant to this study.

Sediment transport, flow calculation and wind speed in the real-space cellular automaton model

In a three dimensional square lattice, we consider three states (i.e., fluid, mobile and immobile sediment). Local interactions between pairs of nearest neighbor cells called doublets are computed in order to simulate the sediment transport (Fig. DR13).

Individual physical processes are isolated as a set of doublet transitions. Each transition is characterized by a rate parameter with the dimension of a frequency. These transition rates introduce into the model the characteristic time scales of the physical mechanisms under consideration (Table DR1).

Neutral cells are used to shape the virtual environment (i.e., bottom topography). In this study, the sedimentary cells are placed on a rotating table to reproduce all types of wind directions, for instance the bidirectional wind regime found in the erg of Fachi-Bilma.

Model parameters

All the transition rates are expressed with respect to the elementary time scale t_0 in such a way that their relative contribution have to be measured from their ratio. For this reason, transition rates for erosion (Λ_0), deposition (Λ_c) and transport (Λ_t) are chosen close to one with $\Lambda_c < \Lambda_0 < \Lambda_t$. Gravity (Λ_g) and diffusion (Λ_d) are occurring over much shorter and longer periods of time, respectively. We chose $\Lambda_d \ll \Lambda_0 \ll \Lambda_g$. $a < 1$ corresponds to the ratio between vertical and horizontal transition rates for erosion and transport; $b > 1$ corresponds to the ratio between deposition rates on flat and rough surfaces.

Elementary units		Units	
l_0	Length	[L]	
t_0	Time	[T]	
τ_0	Stress	$[M][L]^{-1}[T]^{-2}$	

Model parameters		Units	Value
L	System width and length	l_0	[400, 1600]
H	System height	l_0	100
Λ_0	Transition rate for erosion	$1/t_0$	1
Λ_t	Transition rate for transport	$1/t_0$	1.5
Λ_c	Transition rate for deposition	$1/t_0$	0.5
Λ_g	Transition rate for gravity	$1/t_0$	10^5
Λ_d	Transition rate for diffusion	$1/t_0$	0.01
a	Erosion/transport coefficient	1	0.1
b	Deposition coefficient	1	10
$\tau_2 - \tau_1$	Erosion range	τ_0	100

Table DR1: Units and values of the parameters of the model of sediment transport.

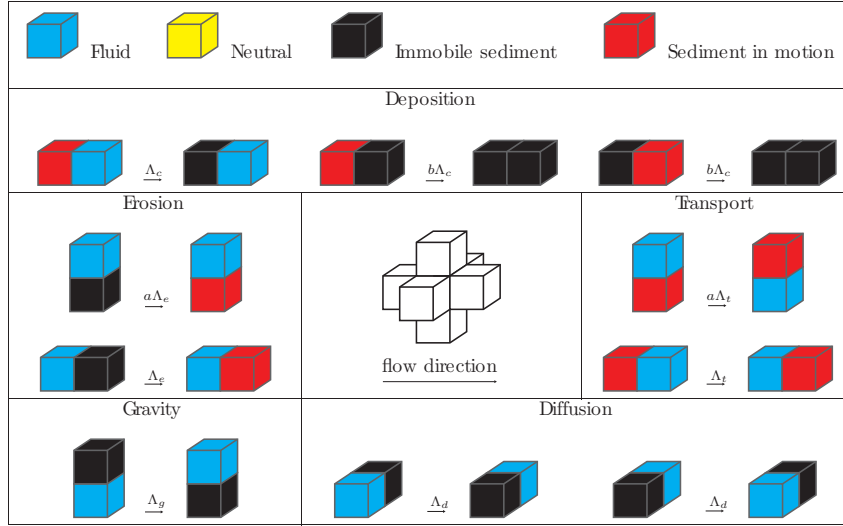


Figure DR13: The three states (fluid, mobile and immobile sediment) and the doublet interactions in the model of sediment transport. Different sets of transition are associated with deposition, erosion, transport, gravity and diffusion. $\{\Lambda_c, \Lambda_e, \Lambda_t, \Lambda_g, \Lambda_d\}$ are transition rates with units of frequency; a and b are constants (see Tab. S1 for the model parameter values). The central inset shows the direction of the flow and the orientation of the nearest neighbors in our regular cubic lattice. Neutral cells are used to shape the virtual environment. Injection/removal cells are used to introduce input/output fluxes of sediment.

We use a two-dimensional lattice-gas model to simulate the flow and calculate the permanent feedback between bed shear stress and topography [6–9]. In the model of sediment transport, the flow is calculated in 2D vertical planes parallel to the direction of the wind and confined by two walls of neutral cells at the top and the bottom of the system.

Using the output of the lattice-gas cellular automaton, we estimate both components of the local velocity field by averaging the velocity vectors of fluid particles over space and time. The flow continuously affects the topography through sediment transport in zones where the basal shear stress is strong enough to mobilize sedimentary particles. In order to determine the effect of flow velocity on the erosion rate Λ_e , we locally compute the bed shear stress from the spatial variation of the tangential velocity profile. In the referential of the topography, it writes

$$\tau_s = \tau_0 l_0 \frac{\partial V_x}{\partial z}, \quad (1)$$

where τ_0 is the stress scale of the model and V_x is dimensionless and expressed as a number of fluid particles. Then, we consider that the erosion rate is linearly related to the bed shear stress τ_s according to

$$\Lambda_e = \begin{cases} 0 & \text{for } \tau_s \leq \tau_1, \\ \Lambda_0 \frac{\tau_s - \tau_1}{\tau_2 - \tau_1} & \text{for } \tau_1 \leq \tau_s \leq \tau_2, \\ \Lambda_0 & \text{else.} \end{cases} \quad (2)$$

where Λ_0 is a constant rate, τ_1 is the threshold for motion inception and τ_2 is a parameter to adjust the linear relationship. By definition, $(\tau_s - \tau_1)$ is the excess shear stress from which we can account for the feedback mechanism of the bed shear stress on the topography.

We can associate changes in τ_1 -values to variations in excess shear stress and therefore to variations in wind shear velocity: the higher the τ_1 -value is, the lower the wind shear velocity is. Then, for all τ_1 -values, we have computed the saturated sand flux on a flat bed and renormalize this flux with respect to its maximum value at $\tau_1 = 0$ (Fig. DR14).

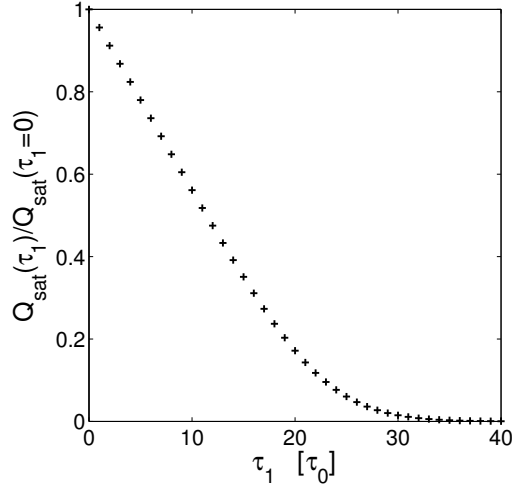


Figure DR14: The saturated flux with respect to the τ_1 -value. $Q_{\text{sat}}(\tau_1)$ is normalized by its maximum value $Q_{\text{sat}}(\tau_1 = 0)$. Note that an increasing τ_1 -value corresponds to a decreasing flow strength and that these changes in τ_1 -value do not affect the spatial and temporal distributions of the bed shear stress τ_s on an arbitrary flat layer of sediment.

Theoretical transport relationships can be expressed as

$$Q_{\text{sat}} = \begin{cases} 0 & \text{if } \tau_s \leq \tau_c, \\ \tau_s^\gamma (\tau_s - \tau_c) & \text{if } \tau_s \geq \tau_c. \end{cases} \quad (3)$$

where γ is a positive (or null) constant and τ_c the shear stress at the onset of erosion [10–14]. Introducing the shear velocity $u_* \propto \tau_s^{1/2}$ (i. e. high Reynolds number) and considering that Q_{sat}^0 is the Q_{sat} -value for $\tau_c = 0$, we can show that

$$\frac{Q_{\text{sat}}}{Q_{\text{sat}}^0} = 1 - \left(\frac{u_c}{u_*} \right)^2. \quad (4)$$

As described below, wind velocity time series allow to calculate the (u_*/u_c) -value in nature and therefore to estimate the corresponding $Q_{\text{sat}}/Q_{\text{sat}}^0$ -value. Considering that we have the same ratio in the model, Eq. 4 and Fig. S14 give the opportunity to estimate the τ_1 -value that we should take in our simulation for scaling purposes. This value corresponds to a given flux of sediment $Q_{\text{sat}}(\tau_1)$ expressed in units of l_0^2/t_0 , where l_0 and t_0 are the elementary length and time scales of the model, respectively. Let us now determine the $\{l_0, t_0\}$ -values.

Length and time scales in the real-space cellular automaton dune model

The elementary length and time scales $\{l_0, t_0\}$ of the real-space cellular automaton dune model are determined with respect to the physical mechanism that select λ_{max} , the characteristic length scales for the formation of dunes in nature (i. e. the most unstable wavelength of a flat sand bed exposed to a fluid flow). Then, in all natural environments where the dune instability can be observed, the l_0 and t_0 -values can be calculated with respect to the magnitude of the parameters that control the λ_{max} -value and the saturated flux of sediment [5, 15–19].

The elementary length scale

Using a linear stability analysis, the characteristic length scale for the formation of dunes in the model, λ_{max} , can be expressed in unit of l_0 and compare to the corresponding length

scale in nature. For arid desert on Earth, [16] have shown that

$$\lambda_{\max} \approx 50 \frac{\rho_s}{\rho_f} d \approx 20 \text{ m},$$

where ρ_s/ρ_f is the grain to fluid density ratio and d the grain diameter. In the cellular automaton dune model, [5] have shown that

$$\lambda_{\max} \approx 40 l_0.$$

Then, the elementary length scale of the real-space cellular automaton dune model is

$$l_0 \approx 0.5 \text{ m}. \quad (5)$$

The elementary time scale and sediment flux

From the meteorological data of Bilma airport (Niger, 18° 41' North, 12° 55' East), we extract the wind speed u^i and the wind direction \vec{x}_i at different times $t_1 \leq t_i \leq t_N$, $i \in [1, N]$. Considering that these wind properties have been measured at a height of $z = 10 \text{ m}$, we calculate the shear velocity

$$u_*^i = \frac{u^i \kappa}{\log(z/z_0)} \quad (6)$$

where $z_0 = 10^{-3} \text{ m}$ is the surface roughness length and $\kappa = 0.4$ is the von-Kármán constant. The mean shear velocity is

$$\langle u_* \rangle = \frac{\sum_{i=2}^N u_*^i \delta_i (t_i - t_{i-1})}{\sum_{i=2}^N \delta_i (t_i - t_{i-1})}, \quad (7)$$

with

$$\delta_i = \begin{cases} 0 & \text{for } u_*^i < u_c, \\ 1 & \text{for } u_*^i \geq u_c. \end{cases}$$

We obtain

$$\langle u_* \rangle = 0.296 \text{ m/s} \quad \text{and} \quad \left\langle \frac{u_*}{u_c} \right\rangle = 1.58$$

using a mean grain size $d = 180 \mu\text{m}$ (see Fig. S4) and the formula of [20],

$$u_c = 0.1 \sqrt{\frac{\rho_s}{\rho_f} g d} = 0.19 \text{ m/s},$$

to determine the threshold shear velocity value for motion inception. Then, we inject this $\langle u_*/u_c \rangle$ -value in Eq. 4 and Fig. S14 to estimate the corresponding τ_1 -value and the corresponding flux of sediment. Here, we have

$$\frac{Q_{\text{sat}}(\tau_1)}{Q_{\text{sat}}(\tau_1 = 0)} = 0.6,$$

$$\tau_1 = 9.4 \tau_0 \quad \text{and} \quad Q_{\text{sat}} = 0.14 l_0^2 / t_0.$$

With the same wind data, we also estimate the sand flux using another relationship proposed by [20],

$$Q_{\text{sat}}(u_*) = 25 \frac{\rho_f}{\rho_s} \sqrt{\frac{d}{g}} (u_*^2 - u_c^2) \quad \text{for } u_* \geq u_c. \quad (8)$$

In practice, we calculate the sand flux vector over a flat sand bed

$$\overrightarrow{Q}_{sat}^i = Q_{sat}(u_*^i) \delta_i \overrightarrow{X}_i.$$

Thus, we estimate the mean sand flux, also called the drift potential,

$$Q = DP = \frac{\sum_{i=2}^N \|\overrightarrow{Q}_{sat}^i\| (t_i - t_{i-1})}{\sum_{i=2}^N (t_i - t_{i-1})} = 30.6 \text{ m}^2/\text{a}, \quad (9)$$

as well as the resultant drift potential

$$RDP = \left\| \sum_{i=2}^N (t_i - t_{i-1}) \overrightarrow{Q}_{sat}^i \right\| = 22.6 \text{ m}^2/\text{a} \quad (10)$$

from the 3rd of September 2000 to the 31st of December 2012 using the wind data from the Bilma airport.

Finally, matching the average saturated flux in the model to the mean saturated flux in the dune field, we obtain

$$t_0 = \frac{Q_{sat}(\tau_1)}{Q} l_0^2 = 1.1 \times 10^{-3} \text{ a} = 0.4\text{d} = 9.7 \text{ h}. \quad (11)$$

Topographic effects on the flux divergence

We examine the impact of a non-erodible topographic obstacle on the formation of dunes and the overall sediment transport under unidirectional and bidirectional wind conditions. All the parameters of the model are set up according to the wind regime observed in the erg of Fachi-Bilma. We fix the value of the threshold shear stress for motion inception (i.e., the τ_1 -value). Thus, according to Eq. 11, the saturated sand flux in the model corresponds to the DP-value in the field (see Eq. 9). For the bidirectional wind regime, we consider a divergence angle of 75° and a transport ratio of 1.5 between the prevailing and the secondary winds. Considering a constant wind strength, only the duration of individual wind varies. As for the wind records from the Bilma airport, the overall wind reorientation cycle has a duration of approximately two months.

Upstream, we consider a constant injection of sediment which is below the saturated flux. Then, without topography (i.e., flat surface), no bedform are generated; the sediment flow over the surface with no accumulation whatever the function of wind directionality. By adding a topography obstacle with an aspect ratio similar to the ones observed in the erg of Fachi-Bilma (see Fig. 1 of the main text and Fig. DR1), bedforms are observed under both wind conditions (i.e., one or two winds) as shown on Fig. DR15. The explanation lies on the divergence of the sediment flux and in the presence of a zone of accumulation on the lee side of the topographic obstacle where the flow decelerates.

Under an unidirectional wind regime, a lee dune develops and breaks up into individual barchan dunes downwind, at a distance where the topographic obstacle has no more effect of the flow. Basically, sediment accumulates in the recirculation zone downstream of the maximum of topography. The situation is different in bidirectional wind regime because the overall deposition/erosion rate should account for the spatial distribution of sediment flux associated with each wind. In this case, deposition is located downstream of obstacles according to the resultant flux direction at the top of these topographic obstacles, a condition which favors the development of a linear dune by pure extension from the incipient lee dune

(see Fig. 4 of the main text and Fig. DR1). In addition, there is a downstream convergence of flux lines over a distance which is proportional to the height of the topographic obstacle (Fig. DR16). These convergent fluxes do not require transverse secondary flows as they simply result from the superposition of sand-transport vectors associated with individual winds.

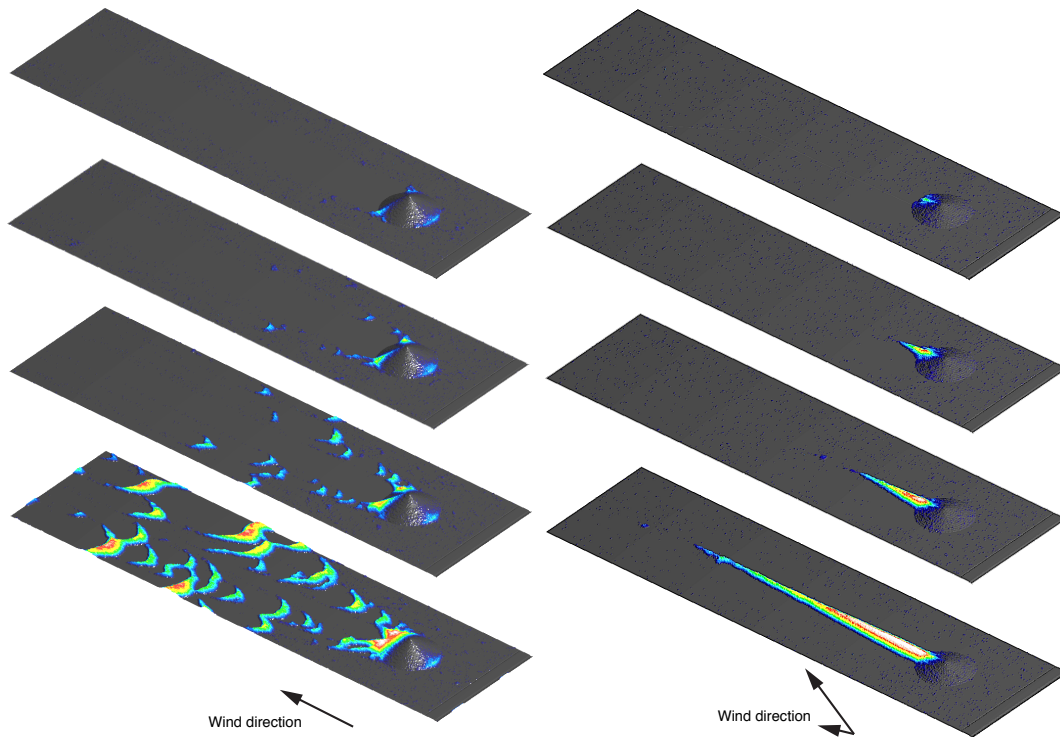


Figure DR15: Dune pattern formation on a non-erodible ground downstream of an obstacle. In both simulations, there is the same sediment input rate below saturation at the upstream border of the cellular space. Without obstacle, no bedforms are observed and the sediment is uniformly transported across the entire system (not shown). As this uniform sediment flux interact with topography bedforms develop. (left) Under a unidirectional wind, deposition occurs in the re-circulation zone downstream of the obstacle. The subsequent lee dune does not extend as the development of the bed instability generates trains of barchan dunes. Note also a small zone of deposition upstream of the obstacle as the pressure gra-dient increases due to the presence of the positive topographic anomaly. (right) Under a bidirectional wind regime (see black arrows), deposition occurs due to the convergence of the sand flux in the lee of the obstacle (see Fig. DR16). From this fixed source, a linear dune develop in the direction of the resultant sand flux (see also Fig. 4 of the main text).

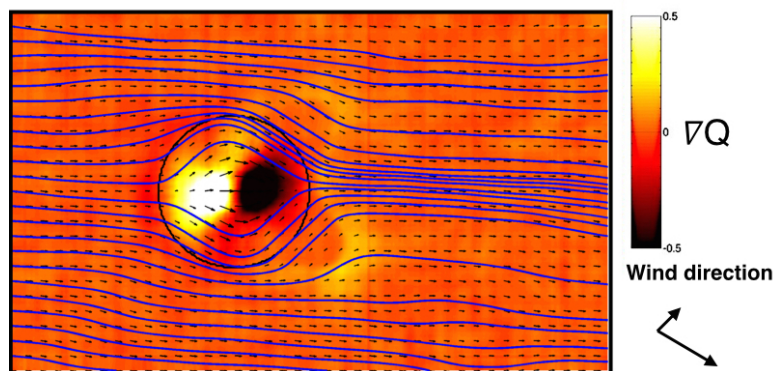


Figure DR16: Sediment flux under bidirectional wind conditions in presence of a topographic obstacle. Sediment flux are shown with black vectors and the corresponding streamlines are shown in blue. Dark and bright areas shows deposition and erosion areas, respectively. Under a bidirectional wind condition, there is clear zone of deposition on the lee side of the obstacle. Note that this deposition area reaches the top of the relief similarly to what observed on the field (see Fig. DR1). The convergence of the sediment flux streamlines, from both sides of the obstacle, feed the incipient finger. Then, the sediment is transported along the dune crest to be deposited at its tip.

References

- [1] Mainguet, M. et al. *L'Erg de Fachi-Bilma (Tchad-Niger): Contribution a la connaissance de la dynamique des ergs et des dunes des zones arides chaudes*. Éd. du Centre national de la recherche scientifique, 1978.
- [2] Moratto, Z. M., et al. Ames stereo pipeline, nasa's open source automated stereogrammetry software. *Lunar and Planetary Science Conference 41*, abstract #2364, 2010.
- [3] de Franchis, C., et al. Automatic sensor orientation refinement of pléiades stereo images. *IGARSS*, 2014.
- [4] Rozier, O. et al. A real-space cellular automaton laboratory. *Earth Surface Processes and Landforms*, 39(1):98–109, 2014.
- [5] Narteau, C., et al. Setting the length and time scales of a cellular automaton dune model from the analysis of superimposed bed forms. *J. Geophys. Res.*, 114(F03006), 2009.
- [6] Frisch, U., et al. Lattice-gas automata for the navier-stokes equation. *Phys. Rev. Lett.*, 56(14):1505–1508, 1986.
- [7] d'Humières, D., et al. Lattice gas models for 3D hydrodynamics. *Europhys. Lett.*, 2(4):291–297, 1986.
- [8] Chopard, B. et al. Cellular automata modeling of physical systems. *Cambridge University Press*, 1998.
- [9] Rothman, D. H. et al. Lattice-gas cellular automata. *Cambridge University Press*, 2004.
- [10] Bagnold, R. A. Flow of cohesionless grains in fluids. *Philos. Trans. R. Soc. London, Ser. A*, 249:235, 1956.
- [11] Anderson, R. et al. Simulation of eolian saltation. *Science*, 241:820, 1988.
- [12] Ungar, J. E. et al. Steady state saltation in air. *Sedimentology*, 34:289–299, 1987.
- [13] Rasmussen, K. R., et al. Saltation and wind flow interaction in a variable slope wind tunnel. *Geomorphology*, 17:19–28, 1996.
- [14] Andreotti, B. A two-species model of aeolian sand transport. *J. Fluid Mech.*, 510:47–70, jul 10 2004.
- [15] Hersen, P., et al. Relevant length scale of barchan dunes. *Physical Review Letters*, 89(26), dec 23 2002.
- [16] Elbelrhiti, H., et al. Field evidence for surface-wave-induced instability of sand dunes. *Nature*, 437:720–723, 2005.
- [17] Charru, F. Selection of the ripple length on a granular bed. *Phys. Fluids*, 18:121–508, 2006.
- [18] Claudin, P. et al. A scaling law for aeolian dunes on Mars, Venus, Earth, and for subaqueous ripples. *Earth Plan. Sci. Lett.*, 252:30–44, 2006.
- [19] Zhang, D., et al. Morphodynamics of barchan and transverse dunes using a cellular automaton model. *J. Geophys. Res.*, 115(F03041), 2010.
- [20] Iversen, J. et al. The effect of wind speed and bed slope on sand transport. *Sedimentology*, 46:723–731, 1999.